Taylor & Francis
Taylor & Francis Group

Vehicle System Dynamics
International Journal of Vehicle Mechanics and Mobility

ISSN: (Print) (Online) Journal homepage: https://www.tandfonline.com/loi/nvsd20

A minimal model to study self-excited vibrations of a tram wheelset in curves with small radius of curvature

Florian Zehetbauer, Johannes Edelmann & Manfred Plöchl

To cite this article: Florian Zehetbauer, Johannes Edelmann & Manfred Plöchl (2023): A minimal model to study self-excited vibrations of a tram wheelset in curves with small radius of curvature, Vehicle System Dynamics, DOI: 10.1080/00423114.2022.2139728

To link to this article: https://doi.org/10.1080/00423114.2022.2139728

Published online: 01 Feb 2023.

VEHICLE SYSTEM DYNAMICS
https://doi.org/10.1080/00423114.2022.2139728

A minimal model to study self-excited vibrations of a tram wheelset in curves with small radius of curvature

Florian Zehetbauer, Johannes Edelmann and Manfred Plöchl

Institute of Mechanics and Mechatronics, TU Wien, Vienna, Austria

ABSTRACT

A wheelset of a rail vehicle may experience stability issues in curves with a small radius of curvature, which are typical for tramway networks. Accompanied self-excited vibrations of the wheelset might be a potential mechanism of adverse wheel polygonization, although a possible relationship between the two phenomena is not addressed here. A basic 2-DOF model, representing a wheelset with non-driven, independently rotating resilient wheels, has been derived from the analysis of simulation results with a more detailed system model to understand the reasons for a possibly unstable motion in a uniform curve. It has been found that a dominating motion in the regime with a negative gradient of the lateral creep force–creepage characteristics is necessary for possible self-excitation but is not sufficient for the considered parameter range. The combination and interaction of the lateral oscillations of the resilient wheel and laterally elastic wheelset axle is essential for amplification. Resulting stable limit cycles can be observed, and influences on corresponding amplitudes are discussed. The lateral flexibility of the wheelset axle appears as an important influence.

ARTICLE HISTORY
Received 20 May 2022
Revised 13 October 2022
Accepted 19 October 2022

KEYWORDS
Falling friction effect; self-excitation; wheelset flexibility; negative damping; railway wheel polygonization

1. Introduction

Mechanisms of possibly harmful wheel polygonization are manifold, and the literature suggests different explanations for different types of rolling stocks. Nielsen et al. reported the state-of-the-art until 2003 in [1,2] and gave a comprehensive classification of railway wheel defects. The paper discussed the reasons for the development of out-of-round railway wheels and the damage they may cause to track and vehicle components. A recent survey on potential causes, consequences, simulation methods, and potential remedies to prevent wheel polygonization was presented in [3], focusing on metro vehicles, locomotives, and high-speed trains in China. Wheel polygonization and rail corrugation, in terms of their characteristics, consequences, causes, and countermeasures in the Chinese high-speed railway system, were addressed in [4].

In [5], initial static and dynamic imbalances of the wheelset as a cause of polygonization at high-speed trains were addressed. Cui et al. [6] reported that low-order polygons may emerge at high-speed trains due to the fixation that supports the wheelset during a

CONTACT Johannes Edelmann johannes.edelmann@tuwien.ac.at

typical wheel re-profiling process. The resulting initially small out-of-roundness (OOR) may then be amplified during rolling. Also, wheel flats may cause or exacerbate wheel polygonization [7].

The majority of researchers believe that wheel polygonization is induced by a 'fixed-frequency' or a 'fixed wavelength' mechanism related to a resonance of the vehicle–track system. The vertical track anti-resonance and P2 resonance were suggested as potential factors of growth in the wheel OOR defects at metro trains [8]. Also, [9], it was concluded from the experimental and numerical investigations that the P2 resonance is a possible root cause of wheel polygonization at metro trains. In [10,11], the formation mechanism of high-order wheel polygonization at high-speed trains was studied. It was found that the rail vertical bending modes between the front and the rear wheels of the bogie play an important role in the dynamic response of the wheel–rail forces and related orders of polygonal wear.

Self-excited vibrations of a wheelset–track system, caused by saturated wheel–rail creep forces due to braking or traction, are a further possible polygonization mechanism at high-speed trains [12].

In [3,13], it was reported that the wavelength of polygonal wheels can be related to the lower bending or torsional modes of the wheelset of different types of railway vehicles. Peng et al. investigated in [14] the influence of the locomotive wheelset flexibility on polygonal wear and concluded that the wheelset flexibility would not dominate railway wheel polygonization in a general sense unless the wheelset flexibility effectively and continuously excites the contact responses. Then, wheel polygonization may be initiated. Fröhling et al. identified in [15] the first torsional eigenmode of a driven wheelset, excited due to saturated adhesion in the longitudinal direction, as a potential cause of wheel polygonization at locomotives.

In [16], remedies to reduce the occurrence of the OOR phenomena at tram wheels were discussed. The authors suggested to improve the technology of manufacturing and assembling the wheel rims. Tram vehicle–track vibration responses in curves were analysed considering excitation from polygonal wheels and track irregularities in [17]. Results revealed that the wheelset flexibility, in particular the first torsional mode and the second bending mode, might affect the vibration characteristics of the rail, car body, and axle-box, and intensify the wheel-rail contact force and creepages.

The above short review on wheel polygonization mechanisms follows from the particular interest to find possible root causes of observed polygonal wheels at a specific tram line, but unfortunately could not provide a clear answer. For this tram line, a technical measurement report indicated that periodic wheelset oscillations of $\sim$ 50 Hz may occur when negotiating curves with a small radius of curvature, typically at speeds of 15–19 km/h [18]. The measured wheel profiles included pronounced orders in the range of 17–20. In a preliminary study, [19], a representative system model applying a multibody dynamics simulation software was set up. The simulation results revealed the possible appearance of self-excited vibrations when negotiating a curve with a small radius of curvature, for example, in reversing loops at rather constant speeds. It was found that the effect from falling friction in the lateral creep force–creepage characteristics is essential for the initiation of these self-excited vibrations. A more detailed understanding of self-excited vibrations with respect to the falling friction characteristics at high lateral creepage, typically for trams, is lacking in scientific literature, also in [19], and will be focused here. An appropriate

minimal model will be introduced to identify key parameters that influence the onset of such self-excited vibrations and subsequent vibrational behaviour.

The observed vibrations show a dominant frequency, which is considered essential for polygonal wear as mentioned above, but an investigation about a possible relation or interaction between observed vibrations and observed polygonal wear has not been conducted so far and is left for future investigations.

In the next Section 2, the curving behaviour typical for trams will be pointed out briefly. It will help to understand the assumptions made for the basic system model introduced in Section 3. Stability analysis of the steady-state (linearised) curving motion will be performed, and conditions for potential (oscillatory) instability and resulting self-excited vibrations will be discussed. Mode shapes and energy balances of these self-excited vibrations will be presented to gain further insight into the effects of key parameters. In particular, the main effects from the saturation of the lateral creep force–creepage characteristics and the influence of the effective stiffness of the wheelset axle on the self-excited vibrations will be revealed. Amplitudes of occurring limit cycles will be found from bifurcation analysis. Also, a simple formula for the prediction of these amplitudes will be given. The findings with the basic system model and respective assumptions will be reviewed with a more detailed system model in Section 4. Finally, concluding remarks will close the paper.

2. Creep forces in curves with small radius of curvature

Curving behaviour of railway vehicles has been studied in detail, e.g. in [20], see also [21]. In this section, the (simplified) characteristic curving behaviour of a two-axle tram bogie on grooved rails at sharp curves, representative of tram network systems, will be briefly recaptured for a better understanding of the basic system model, introduced in the next section.

When a railway vehicle negotiates a curve, the bogie yaws about its vertical axis. As a consequence, the leading wheelset of the bogie tends to move outwards, and the rear wheelset moves inwards. Depending on vehicle speed and radius of curvature, the outer front wheel or both the outer front wheel and the inner rear wheel may be in flange contact, which will be assumed here. Both wheelsets are guided by the bogie frame and are not aligned with the radial direction of the curve. Thus, an angle of attack appears between the rolling direction of the wheels and the tangential direction of the rail. The angle of attack of both wheelsets increases with decreasing curve radius, and its magnitude is larger at the leading wheelset.

Due to the present angle of attack, there is a lateral relative velocity between the wheel and the rail, see Figure 1(a), resulting in large values of lateral creepage at sharp curves. The steady-state lateral creepage is approximately equal to the angle of attack and increases with decreasing curve radius. Respective components in longitudinal and spin directions may contribute as well.

Figure 1(b) shows a normalised lateral creep force–creepage characteristics for dry contact between the wheel and the rail, which is based on Polach's formulation [22] and will be used in the context of the paper. At low values of lateral creepage (I), the developed lateral creep force is about proportional to the lateral creepage. As the lateral creepage increases, the lateral creep forces saturate (II). The peak value depends on the coefficient of friction between the wheel and the rail and on the normal force. As the lateral creepage increases

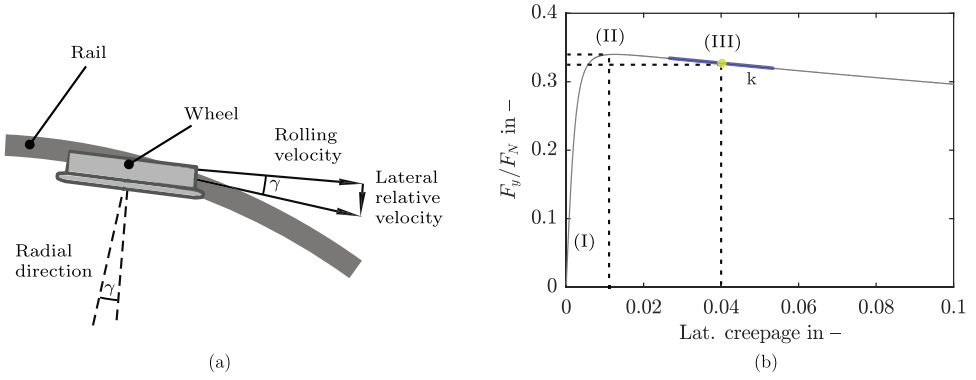

Figure 1. (a) Lateral relative velocity due to angle of attack at outer front wheel in a curve with small radius of curvature. (b) Normalised lateral creep force–creepage characteristics with (I) linear regime, (II) saturated regime, and (III) falling regime.

further and the wheel–rail adhesion level is exceeded, the creep force declines, resulting in a 'falling regime' (III) with a negative gradient. As an explanation for the decreasing creep force, the general decrease of the coefficient of friction with increasing slip velocity due to increasing temperature in the contact patch is given and frequently called 'falling friction effect'. The negative gradient in the falling regime can act as 'negative damping' and may be a source of instability and self-excited vibrations. Basically, a change in the contact conditions, e.g. dry, wet, contaminated contact, rolling velocity, normal load, will modify the characteristics [23].

Necessary conditions to operate in the falling regime of Figure 1(b), related to the relationship between the angle of attack, the curve radius and the vehicle speed at the leading wheelset of a two-axle tram bogie are depicted in Figure 2.

The grey line represents the tram (bogie) operated at the lateral acceleration of 0.65 m/s^2, which is usually the admissible maximum lateral acceleration, for several curve radii. The grey area denotes vehicle speeds above this maximum. A relation between the curve radii and the angles of attack can easily be identified; the angles of attack increase with decreasing curve radii. The coloured lines show only small changes in the angle of attack with varied vehicle speed for a few fixed curve radii. The horizontal black line in Figure 2 represents the angle of attack and the lateral creepage at the wheel–rail adhesion level of the given lateral creep force–creepage characteristics, indicated by (II) in Figure 1(b). For smaller angles of attack, operation in the falling regime of the creep force–characteristic occurs. Then, flange contact at the outer wheel of the leading wheelset (two point contact) or even constrained curving results, as marked in the figure, for smaller curve radii. As this curving configuration is able to promote self-excited vibrations, it will be considered for the modelling approach of the basic system model.

A (not published) technical measurement report indicated that lateral periodic wheelset oscillations, likely from self-excitation, may occur when negotiating particular curves with a small radius of curvature at a speed of about 20 km/h at a particular tramline. Although it is not investigated and confirmed if the observed vibrations can be related to the polygonization of the wheels of order 17–20, the self-excitation phenomenon will be focused on in the remainder of this paper.

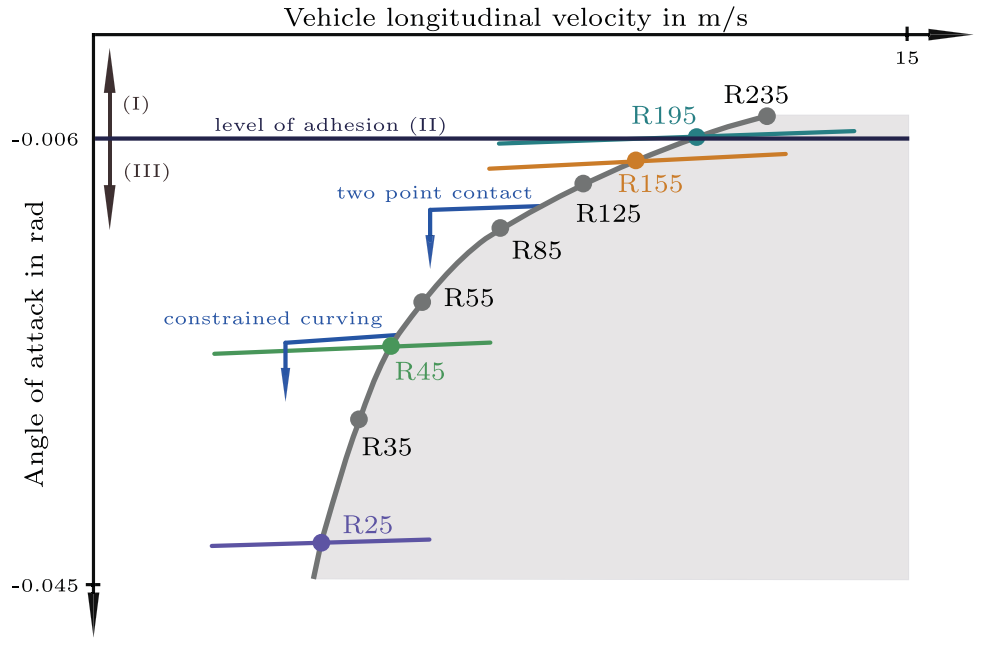

Figure 2. Contact conditions of a two-axle tram bogie at steady-state curving for different radii of curvature and vehicle speeds.

To investigate the influence of system parameters relevant to the appearance of these self-excited vibrations, a system model of a two-axle tram bogie was presented in [19]. This model is briefly described below, as the basic system model, presented in the next section, derives from it. It has also been used to derive the contact conditions of the two-axle tram bogie shown in Figure 2.

A tram is typically composed of a series of driven and non-driven modules. This assembly is separated, and a single, non-driven, low-floor tram vehicle is considered only. The two-axle bogie includes two wheelsets in axlebridge design with independently rotating, resilient wheels. An overview of the generic system is depicted in Figure 3. A corresponding model has been developed in the multibody dynamics simulation software SIMPACK [19]. It has been applied to derive the simulation results in later Section 4.

The car body and the frame of the bogie are modelled by rigid bodies, the primary suspension isolates the wheelsets from the other parts of the tram. These bodies are connected by bushing elements that represent the secondary springs and dampers. The car body is attached to a (virtual) 'traction body' that is moved with constant velocity along the track. The primary suspension connects the wheel axles and the bogie frame and is also modelled utilising bushing elements. To substitute for the omitted fore and aft cars, an additional support of the car body against the inertial system is provided w.r.t. pitch and roll by torsional spring-damper elements.

The flexibility of the wheelsets in the axlebridge design with the independently rotating wheels is accounted for by a linear SIMBEAM element [24]. The wheel hub and the wheel rim of the wheels are represented by rigid bodies, the elastic layer is modelled using a spring-damper element allowing for relative translational and rotational motions of the

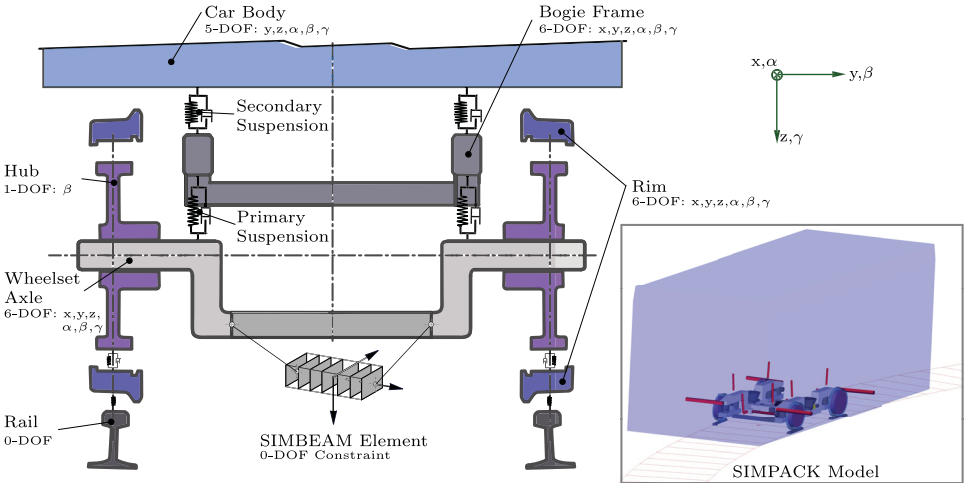

Figure 3. Generic system model in SIMAPCK [19].

rim w.r.t. the hub in several directions. The wheel–rail contact is modelled using Hertzian contact to derive normal forces, and the FASTSIM/Polach algorithm, [22,25], to calculate creep forces, respectively. The flexibility has not been considered.

The authors found in [19] that besides the negative slope of the creep force–creepage characteristics, the flexibility of both the wheelset axle and the resilient wheel is essential for the onset of self-excited vibrations. However, a better understanding of underlying phenomena is still required. This may be obtained from an appropriate minimal model with only small degree of freedom, which is expected to support the understanding of the results from the more detailed system model.

3. Minimal model for self-excited vibrations simulations

As the outer wheel of the leading wheelset of the tram bogie runs in flange contact during the steady-state, constrained curving situation described above, this wheel will be considered to be constantly aligned with the rail, Figure 4. The wheelset is guided by the bogie frame and is, therefore, not aligned with the radial direction of the curve. Thus, an angle of attack γ appears between the rolling direction of the wheels and the tangential direction of the rail.

It is assumed that a lateral motion of the contact point of the inner wheel can be excited by the compliance of the wheelset axle and the resilient wheels, represented in the model by the state variables y_A and y_R. The contribution of these lateral motions to the lateral creepage of the inner wheel will, in general, be small, as the angle of attack will dominate in sharp curves. The considered effective lateral motion y_A may originate from the elasticity of a common axle with two rigid wheels, or it may originate from bending of the elastic support for the two independently rotating wheels, as in our case, see Figure 3. The effective lateral motion of the resilient wheel y_R shall comprise the contributions from camber and lateral displacement. The assumption of resilient wheels will allow for a more comprehensive interpretation, as the motion may easily be locked.

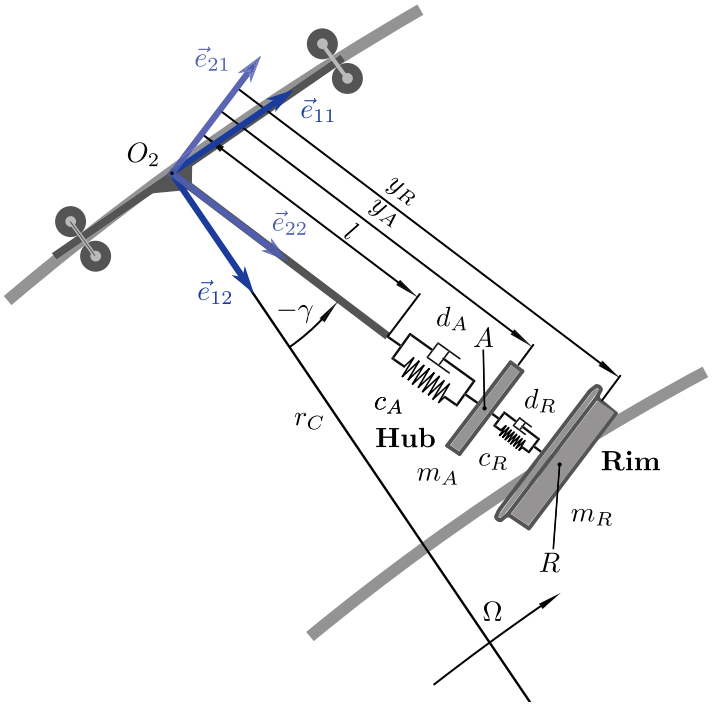

Figure 4. Minimal lateral wheelset model.

All required parameters are denoted in Figure 4. For the lateral motion of the rim w.r.t. the hub, the lumped parameters are the effective stiffness c_R and damping coefficient d_R. The effective stiffness and damping coefficients for the wheelset axle, c_A and d_A, also take a contribution of the stiffness and the damping of the primary suspension into account. The inertia and the mass of the resilient wheel rim are lumped in the equivalent mass m_R. The reduced mass of the wheelset axle and the wheel hub is denoted m_A.

This system model constitutes the most simple but yet fundamental model to study the influences of the falling friction effect and the possible mutual influence of coupled oscillations and their amplification with respect to the lateral dynamic behaviour of the free-rolling wheelset negotiating a sharp curve.

The outer wheel moves along a circular path of radius r_C, representing the outer rail, with constant velocity $\Omega\, r_C$ and yaw rate Ω. Then, the equations of motion read

$$m_A\, a_{A_y} = -c_A(y_A - l) - d_A\, \dot{y}_A + c_R(y_R - y_A) + d_R(\dot{y}_R - \dot{y}_A) \tag{1}$$

$$m_R\, a_{R_y} = -c_R(y_R - y_A) - d_R(\dot{y}_R - \dot{y}_A) - F_y \tag{2}$$

with

$$a_{A_y} = \Omega^2 r_C \cos\gamma - \Omega^2 y_A + \ddot{y}_A, \quad a_{R_y} = \Omega^2 r_C \cos\gamma - \Omega^2 y_R + \ddot{y}_R$$

F_y is the lateral creep force, acting at the wheel–rail contact of the inner wheel. Polach's formulation for the lateral creep force–creepage characteristics, [22], is used. The lateral

creepage ν_y for the inner wheel is given by

$$\nu_y = \frac{\dot{y}_R - V_c}{V_0} \tag{3}$$

with $V_c = \sin\gamma\, V_0 \approx \gamma\, V_0$ and the rolling speed of the inner wheel V_0. The coefficient of friction μ is determined by

$$\mu = \mu_0 \left[(1 - A)\, \mathrm{e}^{-B\nu_y} + A\right] \tag{4}$$

with the ratio of the friction coefficients $A = \mu_\infty/\mu_0$ and the coefficient B of exponential friction decrease; μ_0 is the maximum friction coefficient, μ_∞ is defined at infinite slip velocity. The resulting lateral creep force–creepage characteristics with nominal parameters in later Table 1 are shown in Figure 1(b).

3.1. Stability in first approximation

First, a small perturbation of the steady-states during curving with constant yaw rate Ω and constant angle of attack γ is presumed. Therefore, the equations of motion, (1) and (2), are linearised with respect to the corresponding steady-states in the falling regime (III), denoted by index 0. The linearisation of the lateral creep force–creepage characteristics is determined by gradient k

$$k = k_2 k_3 = \left.\frac{\partial F_y}{\partial \nu_y}\right|_{\nu_{y0}=\gamma} \tag{5}$$

which is illustrated in Figure 1(b). The lateral creep force of the free-rolling inner wheel with rolling speed $V_0 = \Omega(r_C \cos\gamma - y_{R0}) \approx \Omega(r_C - y_{R0})$ results to

$$F_y = F_{y0} + k_2 k_3\, (\nu_y - \nu_{y0}), \quad \nu_y = \dot{y}_R/V_0 - \gamma \tag{6}$$

with parameters k_2, k_3 from Table 1 and more details about them later. y_{R0} is the steady-state lateral distance of the wheel. Then, the linearised equations of motion for small

Table 1. Baseline parameters of the lateral wheelset model.

Symbol	Parameter	Value	Units
r_C	Curve radius at outer wheel	25.75	m
γ	Angle of attack	−0.04	rad
$\Omega\, r_C$	Running speed of the outer wheel	4.15	m/s
F_N	Normal force	35,000	N
m_R	Equivalent mass of wheel rim	125	kg
m_A	Reduced mass of wheelset axle and wheel hub	400	kg
c_R	Effective stiffness coefficient of resilient wheel	4.9×10^7	N/m
d_R	Effective damping coefficient of resilient wheel	9500	Ns/m
c_A	Effective stiffness coefficient of wheelset axle/primary suspension	5.2×10^7	N/m
d_A	Effective damping coefficient of wheelset axle/primary suspension	7250	Ns/m
A	Ratio of friction coefficients μ_∞/μ_0	0.36	–
B	Coefficient of exponential friction decrease	0.7	s/m
μ_0	Coefficient of friction	0.35	–
k_1	Slope parameter for region (I) of creep force-creepage characteristics	0.345	–
k_2	Slope parameter for region (III) of creep force-creepage characteristics	−0.0033	–
k_3	Creep contact parameter	5.8333×10^6	N
ν_{yc}	Critical creep	0.006	–

perturbations $\Delta\underline{y} = \underline{y} - \underline{y}_0$ with state-vector $\underline{y} = [y_A, y_R]^{\mathrm{T}}$ read in matrix notation

$$\mathbf{M}\Delta\ddot{\underline{y}} + \mathbf{D}\Delta\dot{\underline{y}} + \mathbf{C}\Delta\underline{y} = 0 \tag{7}$$

with symmetric matrices

$$\mathbf{M} = \begin{bmatrix} m_A & 0 \\ 0 & m_R \end{bmatrix} \qquad \mathbf{D} = \begin{bmatrix} d_A + d_R & -d_R \\ -d_R & d_R + \dfrac{k_2 k_3}{V_0} \end{bmatrix}$$

$$\mathbf{C} = \begin{bmatrix} c_A + c_R - m_A\Omega^2 & -c_R \\ -c_R & c_R - m_R\Omega^2 \end{bmatrix}$$

The corresponding baseline parameters, which have been derived from the detailed multibody dynamics model to meet the two relevant lateral modes, are listed in Table 1.

With the positive definite mass matrix, a simple, sufficient condition for instability is given by, [26],

$$\mathrm{Tr}(\mathbf{M}^{-1}\mathbf{D}) = \frac{d_A + d_R}{m_A} + \frac{d_R + \frac{k_2 k_3}{V_0}}{m_R} < 0 \tag{8}$$

For a negative gradient $k_2 k_3 < 0$, instability is possible. If (8) holds, and the stiffness matrix $\mathbf{C}$ is positive definite, then the instability will be oscillatory.

The stability behaviour of the minimal lateral wheelset model in first approximation will now be discussed. It will allow to gain insight into the conditions for potential instability as a cause of self-excited vibrations. Based on the characteristic equation of (7), which is of fourth order, stability maps are derived analytically by applying the Routh-Hurwitz criterion [27]. Setting the Hurwitz determinant $H_3 = 0$ and the coefficient of the characteristic equation $a_4 = 0$ yield the oscillatory marginal and monotone marginal stability, respectively. As these expressions are lengthy, they are omitted here and evaluated numerically in Figure 5. Static instability (divergence) arises only for very small parameter values, which are unrealistic from a practical application point of view, and will not be considered any further. The black circle indicates the baseline configuration from Table 1.

In Figure 5(b), the boundaries of stability are presented as a function of the effective stiffness coefficients, c_R and c_A. Obviously, the baseline configuration is dynamically unstable with a diverging oscillation (light grey area) when negotiating a curve of about 25 m with 15 km/h. The effective negative gradient of the lateral creep force–creepage characteristics is essential for this behaviour. However, this condition is not sufficient, as for specific combinations of effective stiffnesses, also stable behaviour may appear due to the coupling of the two relative lateral motions (dark grey area). Their mutual influence will affect the amount of damping. Note, starting from the baseline configuration, a stable behaviour can be achieved if one of the stiffness coefficients tends to infinity ($c_A \to \infty$ or $c_R \to \infty$), i.e. if one of the respective components is considered as rigid. This clearly reveals the implications and the effects of the compliance of the wheelset axle and of the resilient wheel.

The unstable area reduces with the increased effective damping coefficient of the resilient wheel and fully disappears if damping is sufficiently high. In general, damping

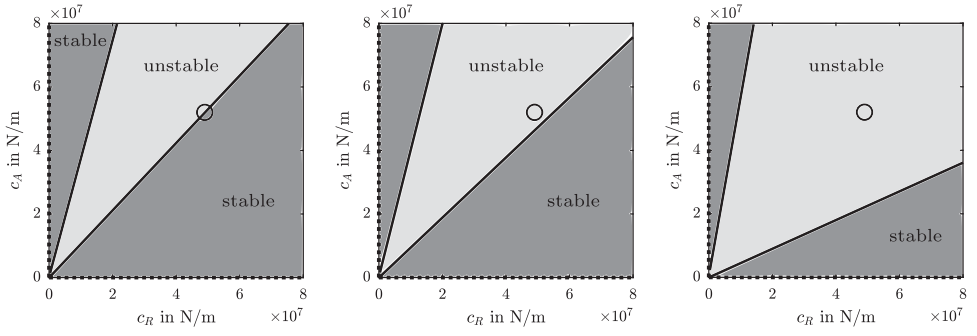

(a) $k_2^* \sim 0.97 \cdot k_2$ (b) Baseline slope k_2 (c) $1.2 \cdot k_2$

Figure 5. Stability maps of minimal lateral wheelset model with an influence of the negative slope in the falling regime of the lateral creep force–creepage characteristics.

effects of the rubber inlay of the resilient wheel will not remain constant over operating time and depend on effects from (pre)load, temperature, and service time [28].

The area of dynamic instability depends significantly on vehicle load, as the gradient of the falling regime of the creep force–creepage characteristics also depends on the normal force. Decreasing the normal force, decreases the negative gradient, [29], i.e. the characteristics become flatter after the peak value, the dynamically unstable area decreases, and the system is less prone to self-excitation, see Figure 5(a)–(c). Without a negative regime, all stiffness combinations are stable as the dynamically unstable area completely vanishes.

If velocity and curve radius are both increased, but lateral acceleration and thus load distribution kept the same as above, the negative gradient in the falling regime increases, [29], due to the increased velocity. As a consequence, the unstable area will increase as well. However, the steady-state lateral creepage will decrease with increasing curve radius and the creep force–creepage characteristics will become flatter depending on the actual curve radius and angle of attack. The stable area will thus increase until the dynamically unstable area completely disappears if the curve radius gets large enough.

Also from $H_3 = 0$, the marginal negative slope $k_2^* \sim 0.97\, k_2$ for the baseline configuration can be derived, which becomes obvious from Figure 5(a). This case is of interest, having in mind that conditioning of the creep force–creepage characteristics by means of friction modifiers might be an option to reduce the risk of self-excitation.

The unstable mode of the baseline configuration oscillates with a frequency of about 50 Hz. The oscillation frequency is dominated by the effective stiffness c_A of the wheelset axle and not by the effective stiffness of the resilient wheel, the radius of curvature, or the vehicle speed. A plot of the root locus for varied c_A is shown in Figure 6, revealing a section of positive conjugate complex eigenvalues corresponding to Figure 5(b). In this section, self-excited vibrations are possible.

3.2. Energy balance and mode shapes

The self-excitation energy and the energy lost from damping in the structural parts and the energy dissipated in the contact between the inner wheel and the rail must balance at the emerging limit cycles of the nonlinear system. As mentioned before, the falling friction

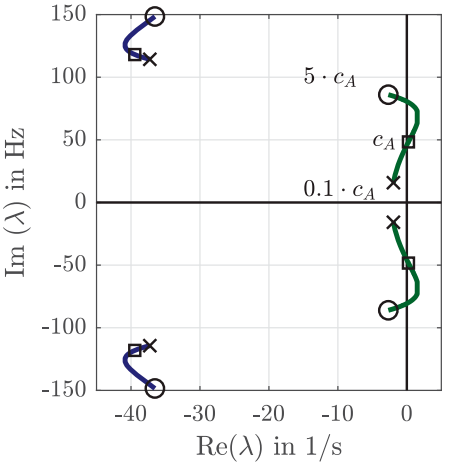

Figure 6. Root locus (poles) for variable effective stiffness coefficient c_A of the wheelset axle in the range from $0.1 \cdot c_A$ (indicated by a cross) to $5 \cdot c_A$ (indicated by a circle).

effect and thus the related negative gradient of the lateral creep force with respect to the creepage can act as a source of self-excitation (energy).

It is assumed that the two components, y_A and y_R, of the periodic oscillatory motion of the wheelset axle that occurs on the boundary of (oscillatory) instability can be described as follows

$$y_A = A\eta \sin(\omega t + \varepsilon) + y_{A0} \quad \text{and} \quad y_R = A \sin(\omega t) + y_{R0} \tag{9}$$

where ω is the dominating radial frequency, A the amplitude, which is assumed to be constant, η the amplitude ratio, and ζ the phase angle between the two lateral motions. If η is zero, only the motion between the rim and the hub is considered.

Considering the periodicity of the displacement and the velocity over one oscillation cycle $\tau = 2\pi/\omega$, the self-excitation energy W is composed of the contribution from the wheel–rail contact, the damping from the resilient wheel and the wheelset axle.

$$W = -\int_0^\tau F_y \dot{y}_R \, \mathrm{d}t - \int_0^\tau d_R(\dot{y}_R - \dot{y}_A)^2 \, \mathrm{d}t - \int_0^\tau d_A \dot{y}_A^2 \, \mathrm{d}t \tag{10}$$

If W is positive, energy is fed into the system and is not fully dissipated over one cycle, and amplitudes of the unstable motion will increase. Integration over one cycle of the periodic oscillation with a constant amplitude and the linear approximation for F_y in (6) yields

$$W = A^2 \omega \pi \left[-d_A \eta^2 - d_R(1 + \eta^2) - \frac{k_2 k_3}{\Omega \left(r_C - y_{R0} \right)} + 2 d_R \eta \cos \varepsilon \right] \tag{11}$$

$W = 0$ will determine the boundary of stability. From (11), it becomes obvious, that for a positive gradient, $k_2 k_3 \geq 0$, W cannot become positive, even for $\cos \varepsilon = 1$. Consequently, the coupled 2-DOF minimal lateral wheelset model cannot self-excite without falling friction effect.

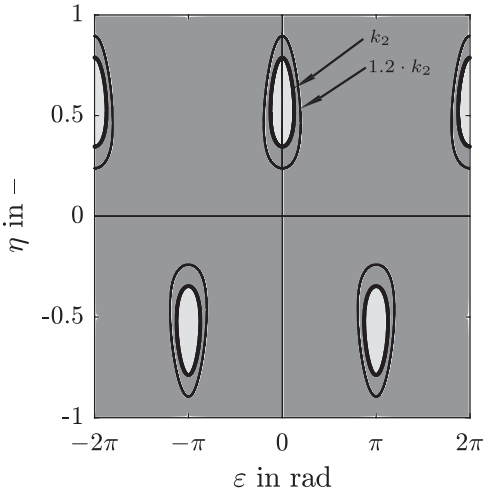

Figure 7. Zero energy boundaries as function of amplitude ratio η and phase angle ε with stable (—) and unstable (—) areas.

However, it has been shown in the previous section that curving in the falling regime is not yet sufficient for the onset of dynamic instability and diverging oscillations. Also, the coupling of the differential equations of the lateral motions plays an important role, determined by the parameters c_j and $d_j, j = A, R$, (if no inertial effects are considered), or by amplitude ratio η and phase angle ε, respectively.

On the boundary of stability, $W = 0$, a relationship between η and ε results from (11); it is plotted in Figure 7 with parameters of the baseline configuration. The boundaries are egg-shaped (thick black lines, marked with k_2) and periodically distributed over the phase angle ε. The mode shapes need to manifest themselves in certain amplitude ratios η and phase angles ε inside the egg (light grey area), where $W > 0$, for possible instability. The stability boundaries do not depend on radial frequency ω here but on vehicle speed $\Omega\, r_C$. For the parameters of the baseline configuration, the steady-state solution will not become dynamically unstable if only the lateral degree of freedom of the wheelset axle ($\eta \to \infty$) or if only the lateral degree of freedom of the wheel rim is introduced ($\eta = 0$).

A comparison of the energy balance between the (stable) 2-DOF system and the (unstable) 1-DOF system (with locked relative motion between the wheel hub and the wheel rim, representing a monobloc wheel) has revealed that for the 2-DOF system, more self-excitation energy is provided and only little energy is dissipated by the additional damper d_R as only a small relative motion ($\dot{y}_R - \dot{y}_A$) appears. However, a large enough negative gradient and/or small enough dissipation may also destabilise the degraded 1-DOF system.

Additionally, the boundaries of stability for the larger negative gradient, $1.2\, k_2$ (thin black lines) corresponding to Figure 5(c), are plotted in Figure 7, indicating a destabilising effect, which becomes obvious from the larger egg-shaped areas. From $W = 0$, also a critical negative slope k_2^c of the lateral creep force–creepage characteristics can be derived, where the eggs and the unstable areas fully disappear, independent of the phase angle ε

$$k_2^c = -\frac{d_R\, d_A\, \Omega\, (r_C - y_{R0})}{k_3 (d_A + d_R)} \tag{12}$$

This simple analytical formula allows to specify $k_2 = k_2^c \sim 0.83\,k_2$, where the stability map in Figure 5 will only show a stable area for all effective stiffnesses c_A and c_R.

3.3. Approximation of the amplitude of the limit cycle

The periodic oscillatory motion of the wheelset axle is characterised by an initial growth of the vibration amplitudes until a stable limit cycle is reached. To study influences on the limit cycles, a closed-form analytical solution for the steady-state amplitude is obtained based on simplifying assumptions and following the approach in [30].

The symmetrical system matrices and the forcing vector from (1) and (2) read

$$\begin{aligned} \mathbf{M} &= \begin{bmatrix} m_A & 0 \\ 0 & m_R \end{bmatrix} & \mathbf{C} &= \begin{bmatrix} c_A + c_R - m_A\Omega^2 & -c_R \\ -c_R & c_R - m_R\Omega^2 \end{bmatrix} \\ \mathbf{D} &= \begin{bmatrix} d_A + d_R & -d_R \\ -d_R & d_R \end{bmatrix} & \underline{F} &= \begin{bmatrix} -m_A\,\Omega^2 r_C \cos\gamma + c_A l \\ -m_R\,\Omega^2 r_C \cos\gamma - F_y \end{bmatrix} \end{aligned} \tag{13}$$

The modal matrix $\mathbf{U}$ of the real eigenvectors $\underline{\tilde{u}}_i$ of the undamped system is obtained from $(\mathbf{C} - \lambda_i \mathbf{M})\underline{\tilde{u}}_i = \underline{0}$ and is used for modal decoupling by introducing modal coordinates in $\underline{Y}$. With

$$\underline{y} = \mathbf{U}\underline{Y} \quad \text{with} \quad \underline{y} = \begin{bmatrix} y_A \\ y_R \end{bmatrix} \quad \underline{Y} = \begin{bmatrix} Y_1 \\ Y_2 \end{bmatrix} \quad \mathbf{U} = \begin{bmatrix} \underline{\tilde{u}}_1 & \underline{\tilde{u}}_2 \end{bmatrix} = \begin{bmatrix} 1 & u_2 \\ u_1 & 1 \end{bmatrix} \tag{14}$$

there follows

$$\mathbf{U}^{\mathrm{T}}\mathbf{M}\mathbf{U}\ddot{\underline{Y}} + \mathbf{U}^{\mathrm{T}}\mathbf{D}\mathbf{U}\dot{\underline{Y}} + \mathbf{U}^{\mathrm{T}}\mathbf{C}\mathbf{U}\underline{Y} = \mathbf{U}^{\mathrm{T}}\underline{F} \tag{15}$$

with diagonal modal mass and stiffness matrix, $\mathbf{M}_{\mathrm{diag}} = \mathbf{U}^{\mathrm{T}}\mathbf{M}\mathbf{U}$ and $\mathbf{C}_{\mathrm{diag}} = \mathbf{U}^{\mathrm{T}}\mathbf{C}\mathbf{U}$, and the modal force vector $\mathbf{U}^{\mathrm{T}}\underline{F}$. The modal damping matrix $\mathbf{U}^{\mathrm{T}}\mathbf{D}\mathbf{U}$ is not diagonal as the eigenvectors of the undamped system are not orthogonal with respect to the damping matrix. It is assumed that structural damping will be small or sufficiently proportional and non-diagonal terms may be neglected [30,31]. The remaining modal damping terms are denoted d_1 and d_2.

The nonlinear lateral creep force–creepage characteristics for the inner wheel will now be approximated by a bilinear curve with slope k_1 for the linear regime and k_2 for the falling regime with

$$F_y = \begin{cases} F_N\left(k_1 \nu_y'\right) & \nu_y' \le 1 \\ F_N\left[k_1 + k_2(\nu_y' - 1)\right] & \nu_y' > 1 \end{cases} \tag{16}$$

ν_y' is the normalised creepage $\nu_y' = (\nu_y k_3)/F_N$. At the critical slip ν_{yc}, there is $\nu_y' = 1$. Implementing (16) in (15) for small oscillations about a constant angle of attack γ yields

$$m_i\ddot{Y}_i + \left(d_i + \frac{k_{Fi}k_{12}}{V_0}\right)\dot{Y}_i + c_i Y_i = 0, \quad i = 1,2 \tag{17}$$

with modal mass m_i, modal stiffness c_i and modal forcing factors $k_{F1} = u_1^2$ and $k_{F2} = 1$. k_{12} represents either the slope $(k_1 k_3)$ in the linear regime or $(k_2 k_3)$ in the falling regime, $V_0 = \Omega(r_C - y_{R0})$ is the rolling speed.

It is well known that the sign of the damping term determines the stability of the respective mode and can be used to find a closed-form analytical expression for the boundary of stability with

$$k_2^s = -\frac{d_2 V_0}{k_3 k_{F2}} = -2V_0 \left\{ c_R^2 [2d_A m_R^2 + d_R (m_A + m_R)^2] + c_A d_R m_R \left[c_A m_R + cm \right] \right.$$
$$\left. - c_R d_R \left[2c_A m_A m_R + (m_A + m_R)\, cm \right] \right\} / \left\{ k_3 k_{F2} \left[c_A m_R + c_R (-m_A + m_R) + cm \right]^2 \right\}$$
$$\text{with} \quad cm = \sqrt{c_R^2 m_A^2 + 2c_R(-c_A + c_R) m_A m_R + (c_A + c_R)^2 m_R^2} \tag{18}$$

The numerical value for k_2^s agrees almost exactly with k_2^*, which was found as numerical solution for the boundary of stability in Section 3.1 for the baseline configuration. It becomes obvious that increasing the effective stiffness of the wheelset axle reasonably leads to lower critical slopes k_2^s, which agrees well with the results gained from the stability map and the results with the more detailed system model in Section 4.

The damping term in (17) also determines the growth or the decay of the vibration amplitudes according to

$$\hat{Y}_i(t) = \hat{Y}_i(0)\, \mathrm{e}^{-(d_i + k_{Fi} k_{12}/V_0) t/(2m_i)} \tag{19}$$

If the exponent becomes negative and the negative damping from the falling friction effect exceeds the positive damping of the structures, self-excitation energy is fed into the system at the wheel–rail contact causing its periodic oscillatory motion to grow exponentially until a steady-state limit cycle amplitude is reached. The oscillations spread into the region with a positive gradient in the creep force–creepage characteristics, thus adding additional damping and reaching an energy balance $W = 0$ over one oscillation cycle $\tau_i = 2\pi/\omega_i$. The shape of steady-state limit cycle can be assumed sinusoidal with $Y_i = A_i \sin(\omega_i t)$, similar to Section 3.2. Then, the energy balance for the limit cycle of the dominant mode

$$W_i = \int_0^{\tau_i} P_i \, \mathrm{d}t = 2 \left(\int_0^{t_c} P_i \, \mathrm{d}t + \int_{t_c}^{\pi/\omega} P_i \, \mathrm{d}t \right) = 0 \quad \text{with} \quad P_i = -F_i \dot{Y}_i - d_i \dot{Y}_i^2 \tag{20}$$

can be derived to, here $i = 2$,

$$W_i = \left[(k_1 - k_2) k_{Fi} \left[4(F_N V_0 + k_3 V_c) \sin(\omega_i t_c) - A_R \omega_i k_3 (2\omega_i t_c + \sin(2\omega_i t_c)) \right] \right.$$
$$\left. - 2\pi A_R \omega_i (k_2 k_3 k_{Fi} + d_i V_0) \right] / (4V_0) = 0 \tag{21}$$

Time t_c and given critical creepage ν_{yc} are related to the transition between the two linear regimes of the lateral creep force–creepage characteristics with

$$\nu_{yc} = \frac{A_R \omega_i \cos(\omega_i t_c) - V_c}{V_0} \tag{22}$$

A closed-form analytical solution for the steady-state amplitude $A_R \omega_i$ of the limit cycle of the wheel rim motion may be obtained from solving Equations (21) and (22), applying a

Taylor series approximation with $\sin(2\omega_i t_c) \approx 2\omega_i t_c - (2\omega_i t_c)^3/3!$, [30],

$$A_R\omega_i \approx \frac{V_0(\nu_{yc}+\gamma)}{\cos(\omega_i t_c)}, \quad \omega_i t_c = \left(\frac{3\pi(k_2k_3k_{Fi}+d_iV_0}{2k_3k_{Fi}(k_2-k_1)}\right)^{1/3} \tag{23}$$

The slope of the falling regime affects both the growth rate and the steady-state amplitude of the oscillatory motion.

Figure 8(a) shows the rise of oscillations $\dot{y}_R(t)$ for the baseline configuration and for the configuration with increased effective stiffness of the wheelset axle, $1.5\,c_A$, based on simulation results with the simplified lateral creep force–creepage characteristics in (16). For the stiffer wheelset, there results an increase of the oscillation frequency from about 50 Hz to 60 Hz. Further, a very fast growth of amplitudes to their constant value can be noticed, both mapped by the simple formulae (19) and (23), while the vibration amplitude of the limit cycle increases only slightly. The fast growth will come to a quick end because of the increased dissipation from the wide extension into the regime with a very large positive gradient of the lateral creep force–creepage characteristics, see Figure 8(b). Note, the oscillations are not symmetrical about the constant angle of attack, $\nu_{y0} = -\gamma$.

3.4. Numerical analysis of the Hopf bifurcation

The behaviour of the nonlinear minimal lateral wheelset model is assessed before and after the loss of stability by means of numerical continuation of the Hopf bifurcation, using the numerical software package MatCont [32]. Polach's nonlinear formulation for the lateral creep force–creepage characteristics, [22], is applied. Model parameters, in particular, the

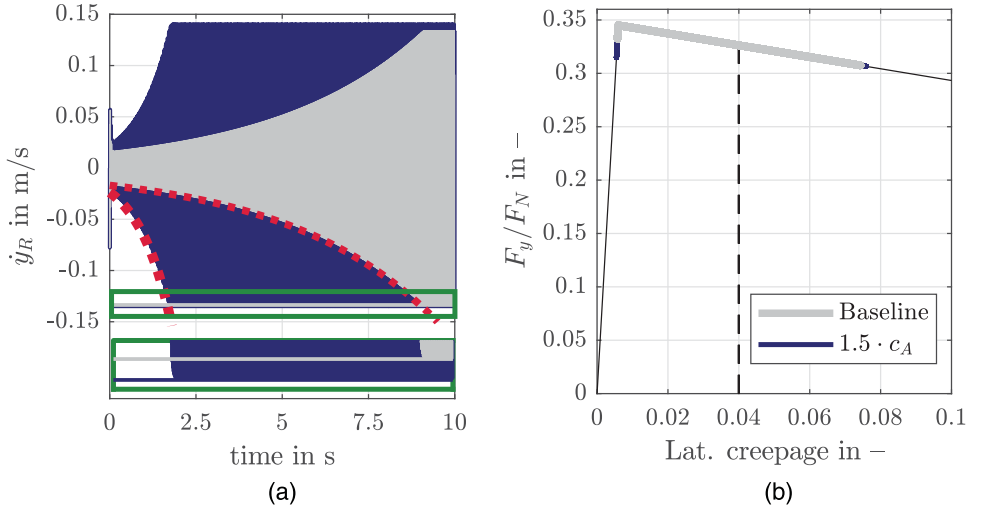

Figure 8. (a) Time history $\dot{y}_R(t)$ of the motion of the wheel rim for the baseline configuration (—) and for $1.5\,c_A$ (—) with detail (green box); corresponding analytical predictions of the amplitude of the limit cycle (horizontal lines in respective colour) and growth of amplitude (- - -). (b) Lateral creep force–creepage characteristics with an exploited range of oscillations (steady-state limit cycles) around $\nu_{y0} = 0.04$ for both configurations.

ratio of friction coefficients A and the coefficient of exponential friction decrease B are listed in Table 1, the parameter A is varied below.

As a distinguished bifurcation parameter, c_A^* the effective stiffness of the wheelset axle is chosen and normalised with the nominal parameter of the baseline configuration; the other parameters remain unchanged. The bifurcation diagram for the motion of the wheel rim y_{R0}^*, normalised with y_{R0}, is displayed in Figure 9(a). The baseline configuration is plotted in green. Between the two supercritical Hopf bifurcation points, at $c_A^* = 0.92$ and $c_A^* = 3.67$, a family of stable periodic solutions (solid line) with small amplitudes are found, which coexists with the unstable steady-state solutions (dashed line). Interestingly, for small and (very) large effective stiffnesses c_A^*, no limit cycles appear; in between, amplitudes do not change significantly, with smaller amplitudes for larger c_A^*. Figure 9(b) reveals that the amplitudes are smaller for the Polach creep force–creepage model compared with the bilinear approximation. The gradients get flatter towards the critical creepage for the Polach model and less self-excitation energy might be fed into the system to balance the dissipated energy even in the falling regime. For the configuration with 1.5 c_A^*, there appears a small overlap to the regime with a positive gradient. Similar to above, higher steady-state amplitudes appear compared with the baseline configuration.

Additionally, in Figure 9(a) parameter A, the ratio of friction coefficients from Polach's model, [22], is varied. With parameter A, the gradient of the lateral creep force–creepage characteristics can be changed. $A = 0.36$ represents the baseline parameter. Only a small variation of the slopes of the falling regime with $A = 0.2$ and $A = 0.4$ is chosen here; see also Figure 11(b). A steeper (negative) gradient, $A = 0.2$, increases both the amplitudes of stable periodic solutions and the range of c_A^* of unstable steady-state solutions responsible for the (stable) limit cycles, which basically confirms the above findings.

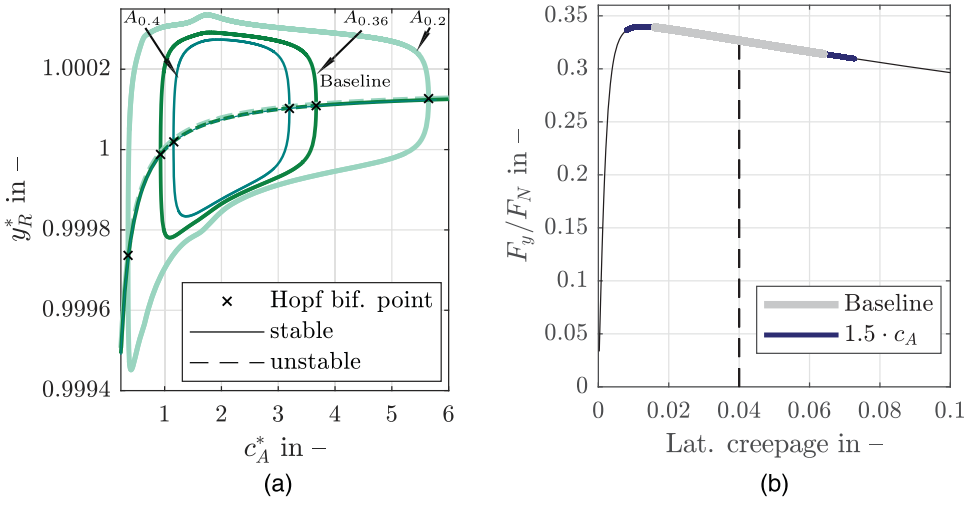

Figure 9. (a) Bifurcation diagram for normalised wheel rim motion y_R^* over normalised effective stiffness c_A^* for creep force–creepage model parameter $A = 0.3$, $A = 0.36$ (baseline parameter), and $A = 0.4$. (b) Lateral creep force–creepage characteristics with an exploited range of oscillations (steady-state limit cycles) around $\nu_{y0} = 0.04$ for the baseline configuration and for 1.5 c_A.

4. Generic system model of two-axle tram bogie

A number of simplifications and assumptions have been made at the minimal lateral wheelset model. Conclusions drawn by means of the minimal model are discussed now by comparing previous findings with results from a detailed generic system model of the two-axle tram bogie described in Section 2.

A systematic nonlinear stability analysis, such as the application of bifurcation theory, is not feasible due to the large level of modelling detail. Instead, significant influences on the limit cycles are presented by time simulation. For the results below, the vehicle initially runs on a straight track and enters a curve (after 3 s) with a constant radius of curvature of 25 m without passing a transition curve. The longitudinal velocity is set to 4 m/s. Thus, the steady-state curving conditions correspond to the studies in the previous sections.

Figure 10(a) shows the influence of the effective stiffness c_A of the wheelset axle on the vibration amplitudes of the inner wheel contact point $\dot{y}_{Rc}$, similar to $\dot{y}_R$. In addition to the baseline configuration, the effective stiffness has been decreased to 0.8 c_A and increased to 1.5 c_A, but also to 4 c_A, which is not realistic for practical application, by adjusting the cross section of the SIMBEAM element. The discontinuity of the curvature after 3 s acts as a disturbance and excites the system, resulting in vibrations. As already seen from the minimal model, increasing the effective stiffness results in faster growth, higher steady-state amplitudes and increased oscillation frequency (around 60 Hz, blue line). Oscillations attenuate, either for decreased effective stiffness (green line) or extreme increase of effective stiffness (brown line). For the self-exited vibration, the analytical formulae (19) and (23) predict similar trends, horizontal lines and dotted red lines, but underestimate the steady-state amplitudes somewhat depending on the quality of the fit of the lateral creep-force–creepage

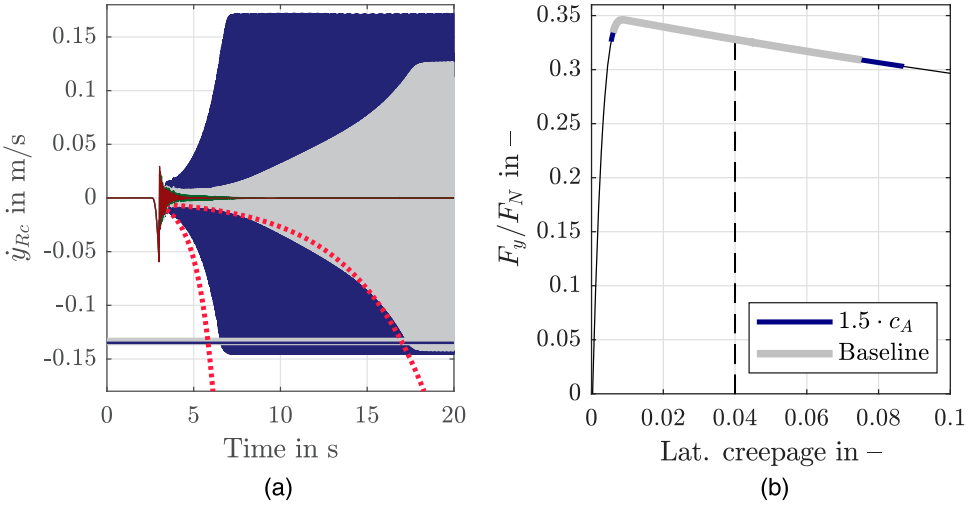

Figure 10. (a) Time history $\dot{y}_{Rc}(t)$ of the lateral motion of the wheel rim contact point for the baseline configuration (—), 1.5 c_A (—), 0.8 c_A (—), 4 c_A (—); corresponding analytical predictions of the amplitude of the limit cycle (horizontal lines in respective colour) and growth of amplitude (- - -). (b) Lateral creep force–creepage characteristics with exploited range of oscillations (steady-state limit cycles) around $\nu_{y0} = 0.04$ for the baseline configuration and for 1.5 c_A.

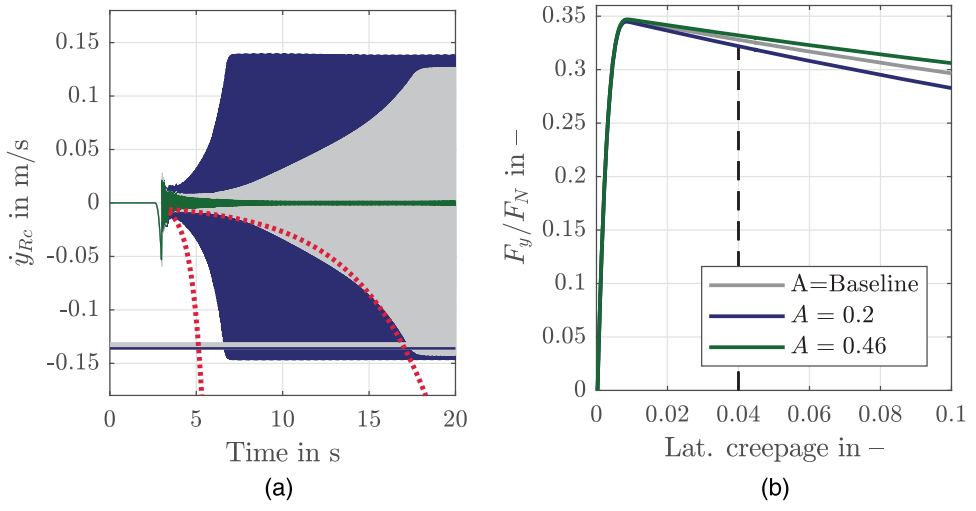

Figure 11. (a) Time history $\dot{y}_{Rc}(t)$ of the lateral motion of the wheel rim contact point for creep force–creepage model parameter $A = 0.2$ (—), $A = 0.36$ (baseline parameter, (—), and (—); corresponding analytical predictions of the amplitude of the limit cycle (horizontal lines in respective colour) and growth of amplitude (- - -). (b) Lateral creep force–creepage characteristics for the three configurations.

characteristic with a bilinear curve. The amplitudes of the limit cycles have increased, Figure 10(b), compared with the minimal model.

The frequency of the self-excited vibrations relates to the stiffness of the wheelset axle and less to the stiffness of the resilient wheel, the radius of the curvature, and the vehicle speed, already found in Section 3.1. The mode shape of the unstable mode can be associated with the second bending mode of the elastic wheelset axle around 50 Hz. In [33], it was found that a continuous excitation with a fixed frequency (such as track irregularity, sleeper passing frequency, etc.), which can fluctuate the contact parameters (normal force, creepages, etc.) in the same frequency, will cause a corresponding order of the wheel polygonization to develop, according to

$$\text{Order} = \frac{\text{Perimeter}}{\text{Wavelength}} = \frac{\text{Frequency}}{\text{Speed}} \times \text{Perimeter} \tag{24}$$

With reference to the report mentioned in the Introduction and considering the dominant frequency of about 50 Hz of the self-excited vibrations and a frequent vehicle speed of about 18 km/h at certain curves with a small radius of curvature of a certain tramline, the corresponding orders match the measured orders of 17–20 quite well. However, it is still questionable if vibrations with respect to self-excitation will dominate wheel polygonization. In general, other potential excitation mechanisms, such as P2 resonance or initial wheel out-of-roundness, might also excite the bending mode of the elastic wheelset axle continuously [3]. The impact of self-excited vibrations on wheel polygonization will depend on their duration and how often they occur. Further, wheel polygonization may not form easily if its wavelength cannot be exactly divided into the wheel circumference [34].

Finally, the influence of the gradient of the lateral creep force–creepage characteristics in the falling regime will be addressed. Similar to Section 3.4, three variants are considered, which are depicted in Figure 11(b). From Figure 11(a), it becomes obvious that the gradient of the falling regime has a significant impact on the stability behaviour of the system. For the negative gradient with $A = 0.46$ (green line), the vibration following the singular disturbance dies out, although the creep force–creepage characteristics is not far from the baseline configuration (grey line). The absolute value of the local gradient at $\nu_y = 0.04$ is smaller than marginal gradient $|k_2^*|$, see Figure 5(a). $A = 0.2$ results in an unstable operating point and leads to a faster growth and higher steady-state amplitudes (blue line), as found before, and suggested by (19) and (23).

In general, it can be concluded that the wheelset axle is less prone to self-excitation with a small gradient of the falling regime as less self-excitation energy is fed into the system.

5. Conclusions

This paper reports on basic research investigating the underlying reasons for self-excited vibrations of wheelsets in curves with small radius of curvature. Respective vibrations cause additional wear. Whether these self-excited vibrations could also be a root cause of adverse wheel polygonization, is left for future research.

A basic minimal lateral wheelset model was introduced to predict the possibility of the onset of self-excitation from stability analysis and to analyse the influence of key parameters on the nonlinear vibrational behaviour and observed limit cycles. Main findings could be confirmed with results from a more detailed generic system model of a two-axle tram bogie.

A falling regime in the lateral creep force–creepage characteristics is necessary but is not sufficient for potential self-excitation for a realistic range of parameters. An interaction of the motions between the resilient wheel and the wheelset axle is essential for potential loss of instability and sustained self-excited vibrations. Results reveal that reducing the effective stiffness of the wheelset axle or the slope of the falling regime in the creep force–creepage characteristics is likely to avoid unstable conditions and suppress subsequent self-excitation. In contrast, increasing the effective stiffness of the wheelset axle in a practically reasonable range may lead to a system behaviour that is more prone to self-excitation. Fast-growing amplitudes of the lateral oscillations of the wheel contact point extend from the falling regime to the regime with a positive gradient, which adds damping, stops the growth of the amplitudes, and leads to a stable limit cycle. The frequency of the unstable mode is governed by the frequency of the wheelset axle stiffness, and the unstable mode is related to a bending mode of the wheelset axle.

Finally, based on various simplifications, analytical formulae have been derived to predict the influence of key parameters on the stability behaviour and on the amplitudes of emerging limit cycles. The validity depends, above all, on the knowledge about the effective lateral creep force-creepage characteristics and on the errors from their bilinear approximation.

Disclosure statement

No potential conflict of interest was reported by the author(s).

References

[1] Nielsen JCO, Johansson A. Out-of-round railway wheels-a literature survey. Proc Inst Mech Eng F J Rail Rapid Transit. 2000;214(2):79–91.
[2] Nielsen JC, Lundén R, Johansson A, et al. Train-track interaction and mechanisms of irregular wear on wheel and rail surfaces. Veh Syst Dyn. 2003;40(1–3):3–54.
[3] Tao G, Wen Z, Jin X, et al. Polygonisation of railway wheels: a critical review. Railw Eng Sci. 2020;28(4):317–345.
[4] Zhai W, Jin X, Wen Z, et al. Wear problems of high-speed wheel/rail systems: observations, causes, and countermeasures in china. Appl Mech Rev. 2020;72(6):060801.
[5] Meinke P, Meinke S. Polygonalization of wheel treads caused by static and dynamic imbalances. J Sound Vib. 1999;227(5):979–986.
[6] Cui D, An B, Allen P, et al. Effect of the turning characteristics of underfloor wheel lathes on the evolution of wheel polygonisation. Proc Inst Mech Eng F J Rail Rapid Transit. 2019;233(5):479–488.
[7] Ye Y, Shi D, Krause P, et al. Wheel flat can cause or exacerbate wheel polygonization. Veh Syst Dyn. 2020;58(10):1575–1604.
[8] Johansson A, Andersson C. Out-of-round railway wheels-a study of wheel polygonalization through simulation of three-dimensional wheel–rail interaction and wear. Veh Syst Dyn. 2005;43(8):539–559.
[9] Tao G, Wen Z, Liang X, et al. An investigation into the mechanism of the out-of-round wheels of metro train and its mitigation measures. Veh Syst Dyn. 2019;57(1):1–16.
[10] Wu X, Rakheja S, Cai W, et al. A study of formation of high order wheel polygonalization. Wear. 2019;424:1–14.
[11] Cai W, Chi M, Wu X, et al. Experimental and numerical analysis of the polygonal wear of high-speed trains. Wear. 2019;440–441:203079.
[12] Zhao X, Chen G, Lv J, et al. Study on the mechanism for the wheel polygonal wear of high-speed trains in terms of the frictional self-excited vibration theory. Wear. 2019;426:1820–1827.
[13] Jin X, Wu L, Fang J, et al. An investigation into the mechanism of the polygonal wear of metro train wheels and its effect on the dynamic behaviour of a wheel/rail system. Veh Syst Dyn. 2012;50(12):1817–1834.
[14] Peng B, Iwnicki S, Shackleton P, et al. The influence of wheelset flexibility on polygonal wear of locomotive wheels. Wear. 2019;432–433:102917.
[15] Fröhling R, Spangenberg U, Reitmann E. Root cause analysis of locomotive wheel tread polygonisation. Wear. 2019;432–433:102911.
[16] Staśkiewicz T, Firlik B, Kominowski J. Out-of-round tram wheels–multibody simulation study based on measured wheel rim geometry. Proc Inst Mech Eng F J Rail Rapid Transit. 2022;236(1):122–133.
[17] Lulu GB, Chen R, Wang P, et al. Random vibration analysis of tram-track interaction on a curve due to the polygonal wheel and track irregularity. Veh Syst Dyn. 2022;60(4):1125–1147.
[18] Lutzenberger S, Isert N. Formation of wheel polygonisation – analysis of influences from a tramway line. Technical Report (not published). 2020.
[19] Zehetbauer F, Edelmann J, Plöchl M, et al. Study on potential evolution mechanisms of oor wheels at trams. In: The IAVSD International Symposium on Dynamics of Vehicles on Roads and Tracks. New York: Springer; 2022. p. 572–581.
[20] Wickens A. Fundamentals of rail vehicle dynamics. Boca Raton (FL): CRC Press; 2003.
[21] Elkins J, Gostling R. A general quasi-static curving theory for railway vehicles. Veh Syst Dyn. 1977;6(2–3):100–106.
[22] Polach O. Creep forces in simulations of traction vehicles running on adhesion limit. Wear. 2005;258(7–8):992–1000.
[23] Vollebregt E, Six K, Polach O. Challenges and progress in the understanding and modelling of the wheel–rail creep forces. Veh Syst Dyn. 2021;59(7):1026–1068.
[24] SIMPACK. [updated 2022 May 12; release 2019]. Available from: https://www.3ds.com/de/produkte-und-services/simulia/produkte/simpack/.

[25] Kalker J. A fast algorithm for the simplified theory of rolling contact. Veh Syst Dyn. 1982;11(1):1–13.
[26] Merkin DR. Introduction to the theory of stability. Vol. 24, Berlin: Springer Science & Business Media; 2012.
[27] Müller PC, Schiehlen W. Linear vibrations: a theoretical treatment of multi-degree-of-freedom vibrating systems. Vol. 7, Berlin: Springer Science & Business Media; 2012.
[28] Šulc P, Pešek L, Bula V, et al. Pre-stressed rubber material constant estimation for resilient wheel application. Adv Eng Softw. 2017;113:76–83.
[29] Spiryagin M, Lee KS, Yoo HH, et al. Modeling of adhesion for railway vehicles. J Adhes Sci Technol. 2008;22(10–11):1017–1034.
[30] Meehan PA. Prediction of wheel squeal noise under mode coupling. J Sound Vib. 2020;465:115025.
[31] Genta G. Vibration dynamics and control. Vol. 616, New York: Springer; 2009.
[32] Dhooge A, Govaerts W, Kuznetsov YA, et al. New features of the software matcont for bifurcation analysis of dynamical systems. Math Comput Model Dyn Syst. 2008;14(2):147–175.
[33] Peng B, Iwnicki S, Shackleton P, et al. A practical method for simulating the evolution of railway wheel polygonalization. In: The dynamics of vehicles on roads and tracks. Boca Raton (FL): CRC Press; 2017. p. 753–758.
[34] Peng B, Iwnicki S, Shackleton P, et al. General conditions for railway wheel polygonal wear to evolve. Veh Syst Dyn. 2021;59(4):568–587.